

Article

Analysis and Suppression of the Cross-Axis Coupling Effect for Dual-Beam SERF Atomic Magnetometer

Fei Lu ^{1,2}, Shuying Wang ^{1,2}, Nuozhou Xu ^{1,2}, Bo Li ^{3,*}, Jixi Lu ^{1,2,3,4}  and Bangcheng Han ^{1,2,3,4}

- ¹ Key Laboratory of Ultra-Weak Magnetic Field Measurement Technology, Ministry of Education, School of Instrumentation and Optoelectronic Engineering, Beihang University, Beijing 100191, China
- ² Beihang Hangzhou Innovation Institute Yuhang, Hangzhou 310023, China
- ³ Hangzhou Extremely Weak Magnetic Field Major Science and Technology Infrastructure Research Institute, Hangzhou 310051, China
- ⁴ Zhejiang Provincial Key Laboratory of Ultra-Weak Magnetic-Field Space and Applied Technology, Hangzhou Innovation Institute, Beihang University, Hangzhou 310051, China
- * Correspondence: boli_9110@163.com

Abstract: Spin-exchange relaxation-free (SERF) atomic magnetometers operated under a near-zero magnetic field are used for vector magnetic field measurements with high sensitivity. Previously, the cross-axis coupling error evoked by a nonzero background magnetic field has been verified to be adverse in modulated single-beam magnetometers. Here, in a dual-beam unmodulated SERF magnetometer, we propose a somewhat different solution model for the cross-axis coupling effect where the field of interest couples with the interference field. Considering two cases where the transverse or longitudinal background field exists, the cross-axis coupling effect dependence on multiple factors is investigated here based on the dynamic response under a background magnetic field within ± 5 nT. The theoretical and experimental investigation suggests that it has an adverse impact on the output response amplitude and phase and tilts the sensitive axis by several degrees, causing a measurement error on the dual-beam magnetometer. To suppress this effect, the background magnetic field is compensated through the PI closed-loop control. The coupling effect is effectively suppressed by 1.5 times at the 10–40 Hz low-frequency band and the sensitivity reaches 2.4 fT/Hz^{1/2}.

Keywords: SERF atomic magnetometer; background magnetic field; transverse dynamic interference field; atomic spin vector; cross-axis coupling; dynamic response



Citation: Lu, F.; Wang, S.; Xu, N.; Li, B.; Lu, J.; Han, B. Analysis and Suppression of the Cross-Axis Coupling Effect for Dual-Beam SERF Atomic Magnetometer. *Photonics* **2022**, *9*, 792. <https://doi.org/10.3390/photonics9110792>

Received: 30 September 2022

Accepted: 21 October 2022

Published: 25 October 2022

Publisher's Note: MDPI stays neutral with regard to jurisdictional claims in published maps and institutional affiliations.



Copyright: © 2022 by the authors. Licensee MDPI, Basel, Switzerland. This article is an open access article distributed under the terms and conditions of the Creative Commons Attribution (CC BY) license (<https://creativecommons.org/licenses/by/4.0/>).

1. Introduction

Optically pumped atomic magnetometers (OPMs) have raised extensive development due to their advantages of high sensitivity [1,2]. Thereinto, atomic magnetometers operated in the spin-exchange relaxation-free (SERF) regime have realized sub-fT measurement sensitivity, becoming the most promising magnetometers for application in biomagnetic measurement, materials characterization, and fundamental physics research [3–9].

Among various application fields of SERF magnetometers, high sensitivity and low measurement error are essential factors for accurate information acquisition of the magnetic field, while their vector property will bring about the cross-axis coupling error due to the nonorthogonal angles and nonzero background magnetic field [10,11]. SERF magnetometers often work under the near-zero magnetic field environment with background magnetic fields shielded and compensated before measurement. However, the background magnetic fields are difficult to maintain at zero due to the magnetic field drift, which will lead to measurement error [12–14], as it also occurs in magnetometers of other principles, such as fluxgate and non-SERF atomic magnetometers [15,16]. In modulated single-beam SERF magnetometers, the gain error and source localization error due to the longitudinal (pump-axis) background magnetic field have been theoretically and experimentally studied [17,18]. Borna et al. [19] proposed the definition of the cross-axis coupling error

and they explored the consequent localization and calibration inaccuracy of OPM-based magnetoencephalography systems, while for the dual-beam unmodulated configuration that possess greater potential to achieve higher sensitivity, a complete solution model for this adverse effect is still lacking. Previously, Jiang et al. revealed the interference effect when there existed a longitudinal background field and transverse (perpendicular to the pump-axis) interference field simultaneously, but they did not explain the potential factors that could influence the output signal, and the condition under a transverse background field was not referred [20]. Actually, we find that in a dual-beam unmodulated SERF magnetometer, there is a cross-axis coupling effect (the output signal contains the magnetic field information of the two orthogonal fields of interest and interference) aroused both along the longitudinal and transverse axes when there are background fields. It has an adverse effect on magnetometers' performance, causing measurement error.

To suppress the cross-axis coupling effect, the triaxial magnetic field should be compensated to zero through active magnetic field compensation [21–24] along with the triaxial magnetic field modulation technology [25–27]. However, the modulation magnetic field of hundreds of nanotesla usually introduces extra spin exchange relaxation and deteriorates the sensitivity of the magnetometer. Hence, it is essential to suppress the coupling effect without damaging the sensitivity. Seltzer et al. proposed a triaxial SERF magnetometer working based on the quasi-static response. However, the sensitivity was of the order of 1 pT/Hz^{1/2} for operation under the unshielded environment [28]. Hereinafter, the quasi-static response is used for suppression of the cross-axis coupling effect under the SERF regime with magnetic shielding, which is realized through the closed-loop control technique.

In this study, the performance of the orthogonal dual-beam SERF magnetometer under the background and interference magnetic fields is analyzed. The cross-axis coupling effect dependence on multiple factors, such as the magnitude and frequency of the background and interference magnetic fields, is measured and the adverse influence on the output signal of the magnetometer is verified. Based on the analysis, the coupling effect can be effectively suppressed by 1.5 times at 10–40 Hz through the closed-loop control of the background magnetic field.

2. Methods

For atomic magnetometers working in the SERF regime, the electron spin vector **S** evolution of the ground state alkali-metal atoms can be described by the Bloch equation [29]:

$$\frac{d}{dt}\mathbf{S} = \frac{1}{q}\left[\gamma_e\mathbf{B} \times \mathbf{S} + R_{op}\left(\frac{1}{2}\mathbf{s} - \mathbf{S}\right) - \Gamma\mathbf{S}\right], \quad (1)$$

where q denotes the nuclear slowing down factor, which is polarization-related, **B** is the magnetic field vector, $\gamma_e \approx 2\pi \times 28$ Hz/nT is the gyromagnetic ratio of the electron, R_{op} is the optical pumping rate, **s** is the photon spin vector along the pump laser ($s = \pm 1$ for a $\sigma \pm$ pumping laser), and Γ is the spin relaxation rate.

Assign that the pump and probe lasers are oriented along the z - and x -axes, respectively. The magnetic field of interest is along the y -axis. Denote $\mathbf{S} = (S_x, S_y, S_z)^T$ and $\mathbf{B} = (B_x(t), B_y(t), B_z(t))^T = (B_{x0} + \delta B_x, B_{y0} + \delta B_y, B_{z0} + \delta B_z)^T$, where B_{x0} , B_{y0} , and B_{z0} are static background magnetic fields. δB_x , δB_y , and δB_z denote the dynamic fields. Under the low-frequency near-zero magnetic field ($\gamma_e |\mathbf{B}| \ll (R_{op} + \Gamma)$ ($\gamma_e \times 3.6$ nT in our system)), the atomic spin vector along the x -axis detected by the probe laser is given by the steady-state solution of Equation (1):

$$S_x = \frac{R_{op}\left[\Gamma'\gamma_e B_{y0} + \Gamma'\gamma_e \delta B_y + \gamma_e^2 B_{x0} B_{z0} + \gamma_e^2 B_{x0} \delta B_z + \gamma_e^2 B_{z0} \delta B_x + \gamma_e^2 \delta B_x \delta B_z\right]}{2\Gamma'\left[\Gamma'^2 + \gamma_e^2 (B_{x0} + \delta B_x)^2 + \gamma_e^2 (B_{y0} + \delta B_y)^2 + \gamma_e^2 (B_{z0} + \delta B_z)^2\right]}, \quad (2)$$

where $\Gamma' = R_{op} + \Gamma$ are introduced. Assuming B_{x0} , B_{y0} , and B_{z0} are zeroed and there are no other interference fields imposed along the x - and z -axes, we can obtain:

$$S_x \approx G_{y0} \delta B_y, \tag{3}$$

where G_{y0} is defined as the scale factor for the input δB_y . It can be expressed as

$$G_{y0} = \gamma_e R_{op} / 2\Gamma'^2. \tag{4}$$

However, if the magnetometer works under the background magnetic fields B_{x0} or B_{z0} , the Larmor precession frequency due to $\gamma_e B_{x0}$ and $\gamma_e B_{z0}$ is nonnegligible compared to Γ' . The B_{x0} - and B_{z0} -relative terms in Equation (2) cannot be ignored, which will have an unexpected effect on the output signal. Figure 1a shows the atomic spin vector evolution under zero magnetic field. An applied δB_y precesses the initial spin vector S_{z0} into the x - z plane, inducing spin vector projection S_x along the x -axis. Hence, the magnetometer is sensitive to δB_y ; in Figure 1b, suppose that there is a background magnetic field B_{x0} and biaxial input δB_y and δB_z ; then, S_x will contain the information of both input fields. We call this the cross-axis coupling effect between y - and z -axes, accounting for the term $(\Gamma' \gamma_e \delta B_y + \gamma_e^2 B_{x0} \delta B_z)$ in the numerator of Equation (2); the same coupling effect is aroused between y - and x -axes (term $\gamma_e^2 B_{z0} \delta B_x$) when B_{z0} exists, as shown in Figure 1c.

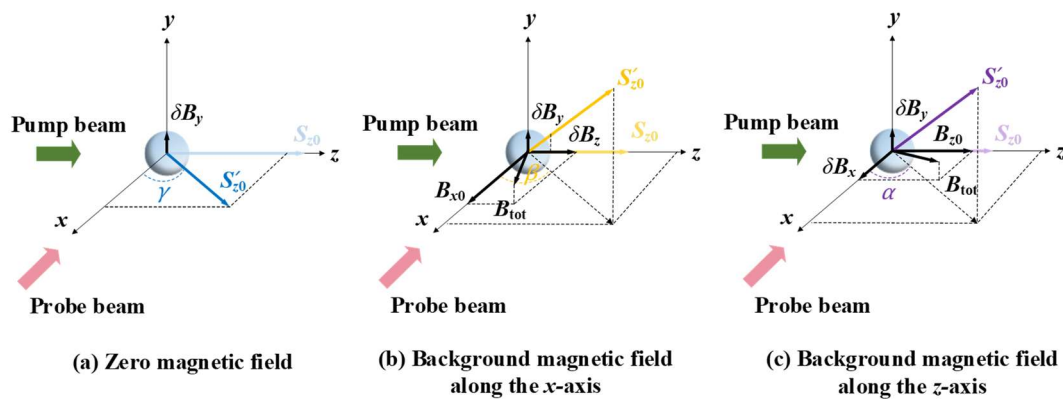


Figure 1. Atomic magnetometer spin vector evolution in (a) zero field and (b,c) background magnetic field. B_{tot} is the composite vector field along the x -, y -, and z -axes. S_{z0} and S_{z0}' denote the initial spin vector aligned by the pump laser and the steady-state spin vector under the magnetic field.

In this study, we consider the coupling terms $(\Gamma' \gamma_e \delta B_y + \gamma_e^2 B_{x0} \delta B_z + \gamma_e^2 B_{z0} \delta B_x + \gamma_e^2 \delta B_x \delta B_z)$ in Equation (2) when the background and interference fields alternate between the x - and z -axes. Hereinafter, the cross-axis coupling effects between z - and y -axes (under B_{x0}), and x - and y -axes (under B_{z0}) are analyzed.

2.1. Cross-Axis Coupling Effect between z - and y -Axes under B_{x0}

First, we consider the case where the background magnetic field is along the x -axis. The vector magnetic field is expressed as $\mathbf{B} = (B_{x0}, \delta B_y, \delta B_z)^T$. With B_{y0} and B_{z0} zeroed, Equation (2) can be simplified as

$$S_x = G_{y1} \delta B_y + G_z \delta B_z. \tag{5}$$

It can be seen that both δB_y and δB_z contribute to the output S_x . δB_y is viewed as the field of interest and δB_z is the interference field. G_{y1} and G_z are the scale factors for the two fields, respectively, and they are given as

$$\begin{cases} G_{y1} = \frac{R_{op} \gamma_e}{2[\Gamma'^2 + \gamma_e^2 B_{x0}^2 + \gamma_e^2 (\delta B_y)^2 + \gamma_e^2 (\delta B_z)^2]} \\ G_z = \frac{R_{op} \gamma_e^2 B_{x0}}{2\Gamma' [\Gamma'^2 + \gamma_e^2 B_{x0}^2 + \gamma_e^2 (\delta B_y)^2 + \gamma_e^2 (\delta B_z)^2]} \end{cases}. \tag{6}$$

Seen from the denominator of G_{y1} in Equation (6), B_{x0} and δB_z result in the decrease in the scale factor for δB_y . Moreover, even if there is no input magnetic field along the sensitivity axis, i.e., $\delta B_y = 0$, there is a nonzero output for S_x , causing measurement error for the magnetometer. Hence, we find that the B_{x0} and δB_z affect the output by changing the sensitivity and tilting the sensitive axis of the magnetometer. The tilting degree is expressed as [19]

$$\varphi_{z,y} \approx \arctan(G_z/G_{y1}). \tag{7}$$

To obtain the output signal under the periodic input signal, the dynamic response is analyzed, and the dynamic fields δB_x , δB_y , and δB_z are expressed with a cosinusoidal signal. Assign $\mathbf{B} = (B_{x0}, B_y \cos(\omega_y t + \varphi_{y0}), B_z \cos(\omega_z t + \varphi_{z0}))^T$, where φ_{y0} and φ_{z0} are initial input phases. The dynamic solution along the x -axis is given as:

$$S_x^{AC} = A_y \sin(\omega_y t + \varphi_{y0} + \theta_y) + A_z \sin(\omega_z t + \varphi_{z0} + \theta_z) + o[\omega(\omega_y, \omega_z)], \tag{8}$$

where $A_y = \frac{S_{z0} \gamma_e B_y}{\sqrt{\Gamma'^2 + q^2 \omega_y^2}}$ and $A_z = \frac{S_{z0} \gamma_e^2 B_z B_{x0} \sqrt{q^2 \omega_z^2 / \Gamma'^2 + 1}}{(\Gamma'^2 + q^2 \omega_z^2)}$ denote the amplitude responses corresponding to the fields of interest and interference. $\theta_y = \arctan(\Gamma' / q \omega_y)$ and $\theta_z = \arctan[\Gamma' / (q \omega_z)]$ denote the output phase delay relative to input initial phase. $O[\omega(\omega_y, \omega_z)]$ are the higher-order terms in the other frequency component that is not included in this discussion. S_{z0} is the steady-state spin vector obtained when the transverse magnetic field has little effect on the atomic spin polarization ($\gamma_e B_{x0} \ll \Gamma'$). By extraction of the frequency-related components for y - and z -axes from the output signal, the cross-axis coupling coefficient for z - and y -axes responses is defined as

$$C_{z,y} = A_z / A_y = \gamma_e B_{x0} \frac{B_{z1}}{B_{y1}} \frac{\sqrt{\Gamma'^2 + q^2 \omega_y^2}}{\Gamma'^2 + q^2 \omega_z^2}. \tag{9}$$

Actually, when $\gamma_e B_{x0}$ is increased and comparable with Γ' , its influence on the spin polarization cannot be ignored anymore. On this occasion, the analytic solution for the Bloch equation is no longer accessible, and there will be nonlinear terms related with B_{x0} that are added in S_{z0} and A_y , which will be verified in the experiments, while they are not given here with analytic expression.

2.2. Cross-Axis Coupling Effect between x - and y -Axes under B_{z0}

Here, the background magnetic field is assumed to be along the z -axis. The vector magnetic field is expressed as $\mathbf{B} = (\delta B_x, \delta B_y, B_{z0})$. With B_{x0} and B_{y0} zeroed, there is

$$S_x = G_{y2} \delta B_y + G_x \delta B_x, \tag{10}$$

The magnetometer is simultaneously sensitive to δB_y and δB_x . The scale factors are given as

$$\begin{cases} G_{y2} = \frac{R_{op} \gamma_e}{2[\Gamma'^2 + (\gamma_e^2 B_x)^2 + (\gamma_e^2 B_y)^2 + (\gamma_e^2 B_{z0})^2]} \\ G_x = \frac{R_{op} \gamma_e^2 B_{z0}}{2\Gamma'[\Gamma'^2 + (\gamma_e^2 B_x)^2 + (\gamma_e^2 B_y)^2 + (\gamma_e^2 B_{z0})^2]} \end{cases}. \tag{11}$$

The magnetic fields B_{z0} and δB_x result in the decrease in the scale factor for δB_y , as seen from the denominator of G_{y2} . It also reveals that even if there is no input δB_y , the output of the magnetometer is not zero, causing measurement error. The tilting degree is

$$\varphi_{x,y} \approx \arctan(G_x/G_{y2}). \tag{12}$$

For solution of the dynamic response, set the total magnetic field as $\mathbf{B} = (B_x \cos(\omega_x t + \varphi_{x0}), B_y \cos(\omega_y t + \varphi_{y0}), B_{z0})$, where φ_{x0} and φ_{y0} are initial input phases. The dynamic solution is [20]

$$S_x^{AC} = A_x \sin(\omega_x t + \varphi_{x0} + \theta_x) + A_y \sin(\omega_y t + \varphi_{y0} + \theta_y), \tag{13}$$

where $A_x = \frac{S_{z0} \gamma_e^2 B_{z0} B_x}{\sqrt{(\Gamma'^2 - \gamma_e^2 B_{z0}^2 + q^2 \omega_x^2)^2 + 4\Gamma'^2 \gamma_e^2 B_{z0}^2}}$ and $A_y = \frac{S_{z0} \gamma_e B_y \sqrt{\Gamma'^2 + q^2 \omega_y^2}}{\sqrt{(\Gamma'^2 - \gamma_e^2 B_{z0}^2 + q^2 \omega_y^2)^2 + 4\Gamma'^2 \gamma_e^2 B_{z0}^2}}$ denote the amplitude responses to the fields of interference and interest. $\theta_x = \arctan\left(\frac{\Gamma'^2 + \gamma_e^2 B_{z0}^2 - q^2 \omega_x^2}{2q\omega_x \Gamma'}\right)$ and $\theta_y = \arctan\left[\frac{\Gamma'(\Gamma'^2 + \gamma_e^2 B_{z0}^2 + q^2 \omega_y^2)}{q\omega_y(\Gamma'^2 - \gamma_e^2 B_{z0}^2 + q^2 \omega_y^2)}\right]$ denote the output phase delay relative to the input initial phase. The cross-axis coupling coefficient is defined as

$$C_{x,y} = A_x / A_y = \frac{\gamma_e B_{z0}}{\sqrt{\Gamma'^2 + q^2 \omega_y^2}} \frac{B_{x1}}{B_{y1}} \frac{\sqrt{(\Gamma'^2 - \gamma_e^2 B_{z0}^2 + q^2 \omega_y^2)^2 + 4\Gamma'^2 \gamma_e^2 B_{z0}^2}}{\sqrt{(\Gamma'^2 - \gamma_e^2 B_{z0}^2 + q^2 \omega_x^2)^2 + 4\Gamma'^2 \gamma_e^2 B_{z0}^2}}. \tag{14}$$

According to Equation (2), the two cross-axis coupling terms ($\gamma_e^2 B_{x0} \delta B_z + \gamma_e^2 B_{z0} \delta B_x$) reveal that the background and interference fields render the cross-multiplication relationship. Hence, the coupling effect can be suppressed by compensating the background magnetic fields B_{x0} and B_{z0} to zero and the coupling terms can be eliminated. Then, Equation (2) is evolved into

$$S_x' = \frac{R_{op} [\Gamma' \gamma_e \delta B_y + \gamma_e^2 \delta B_x \delta B_z]}{2\Gamma' [\Gamma'^2 + \gamma_e^2 (\delta B_x)^2 + \gamma_e^2 (\delta B_y)^2 + \gamma_e^2 (\delta B_z)^2]}. \tag{15}$$

Equation (15) reveals that the output signal is still influenced by the interference magnetic field (seen from the term $\gamma_e^2 \delta B_x \delta B_z$) even if the background magnetic field is compensated, presenting a better suppression consequence under a smaller interference magnetic field. Subsequently, the background magnetic field will be compensated through closed-loop control and the verification experiments will be carried out.

3. Experimental Setup and Procedure

The schematic for the experimental setup is shown in Figure 2. A spherical vapor cell with an outer diameter of 10 mm is used as the sensing element, containing potassium (K), 10 Torr N₂ as the quenching gas, and 700 Torr ⁴He as the buffer gas. To maintain a high-temperature environment, the cell is placed in a ceramic oven, which is attached with flexible polyimide-twisted coils driven by a 100 kHz alternating current. Here, the operating temperature is 18 °C, and the corresponding K atoms density in the cell is about 6.1 × 10¹³/cm³. The magnetometer is integrated into a compact configuration residing in a cylindrical magnetic shield. The magnetic shield consists of an outer four-layer μ-metal to attenuate the Earth’s magnetic field and an inner one-layer ferrite shield with higher resistivity to further reduce the magnetic noise, providing a low-field environment with a residual field of several nanotesla and magnetic noise below 1 fT/Hz^{1/2} [30,31]. A set of triaxial coils (*x*-axis: Helmholtz coils; *y*- and *z*-axes: saddle coils) are mounted inside the shield. The coils are driven by function generators (33500B, Keysight), through which the residual magnetic field is compensated and the desired field is applied. Due to the magnetic eddy interference effect caused by the close distance between the coils and ferrite magnetic shield, the coils constants are recalibrated using a fluxgate before operation.

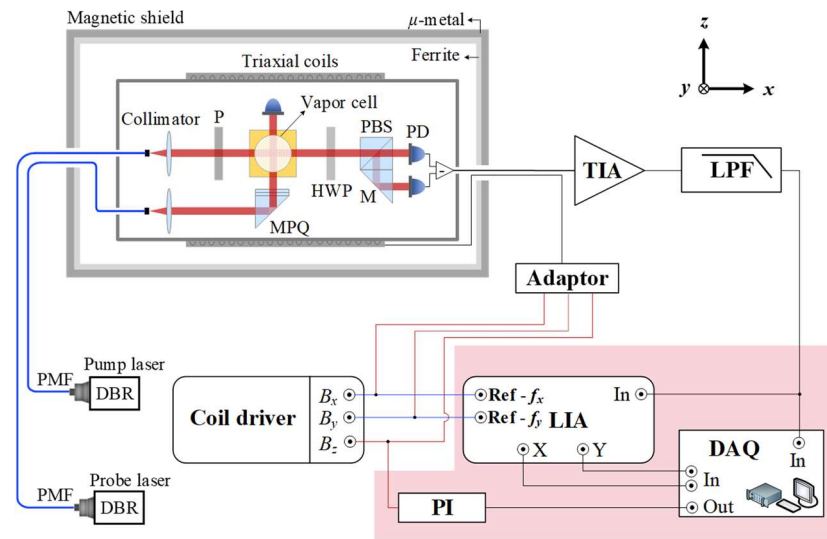


Figure 2. Experimental setup. PMF: polarization-maintaining fiber. P: polarizer. MPQ: M (mirror) + P + QWP (quarter-wave plate). HWP: half-wave plate. PD: photodetector. PBS: polarized beam splitter. TIA: trans-impedance amplifier. LPF: low-pass filter. LIA: lock-in amplifier. PI: proportional-integrative control modules. DAQ: data acquisition system.

Both the pump and probe lasers are generated by distributed Bragg reflector (DBR) lasers with a collimated $1/e^2$ waist diameter of 2.7 cm. The circularly polarized pump laser used to polarize the K atoms is detuned to the center of the pressure-broadened D1 line of 770.10638 nm and the linearly polarized laser used to probe the atomic polarization is 120 GHz blue detuned from the D1 line.

For the magnetic field measurement and control, the polarization change underwent by the probe laser along the x -axis is measured via balanced polarimetry. Thereafter, a trans-impedance amplifier is used to amplify the detected photodetector signal and transfer it into the voltage signal. Then, the voltage signal is collected and processed by a DAQ and demodulated via a LIA and used for subsequent PI closed-loop control.

The cross-axis coupling effect between z - and y -axes (under B_{x0}), and x - and y -axes (under B_{z0}) is studied in the background magnetic field of 0–5 nT (the typical operation range for SERF magnetometers). By collection of the output phase and the amplitude of the sensitive field δB_y , and interference fields δB_x and δB_z via a LIA, the performance of the magnetometer is evaluated. Then, the amplitude and tilting degree for δB_y dependence on the frequency is measured. Finally, the cross-axis coupling effect is suppressed through the dynamic compensation of the background magnetic field.

4. Results and Discussion

4.1. Cross-Axis Coupling Coefficient and Tilting Degree Measurement

To illustrate how the background magnetic fields B_{x0} and B_{z0} influenced the output signal, a static magnetic field ranging from -5 to $+5$ nT was successively applied along the x - and z -axes, respectively. The experimental parameters were set as $f_y = \omega_y/2\pi = 30.5$ Hz, $f_i = \omega_i/2\pi = 20$ Hz, $\varphi_{i0} = 0$ ($i = x, z$), and $B_{j-rms} = 10$ pT (root-mean-square value for dynamic sinusoidal signal, $j = x, y, z$). Through a low-noise LIA, the response amplitude A_j and phase θ_j of the output signal at 30.5 Hz and 20 Hz were extracted, respectively.

Figure 3a shows the biaxial input signals (along the y - and x -axes) and the output signal under the background magnetic field B_{z0} . Seen from the frequency domain, both input signals contributed to the output signal. The same was true under B_{x0} . For the signal of interest B_y , it can be seen from Figure 3b that the response amplitude A_y showed an approximate absorption curve with increasing $|B_{x0}|$, which was mainly caused by the atomic spin polarization S_{z0} precession, while it would not come up under the longitudinal field B_{z0} , because the spin polarization precession only occurred when there was an orthog-

onal magnetic field component. When B_{z0} was applied, A_y increased, indicating a typical magnetic resonance tendency evoked by B_{z0} and f_y . The increased coupling coefficients $C_{z,y}$ and $C_{x,y}$ indicated a stronger cross-axis coupling effect with increasing background field, which was consistent with Equations (9) and (14).

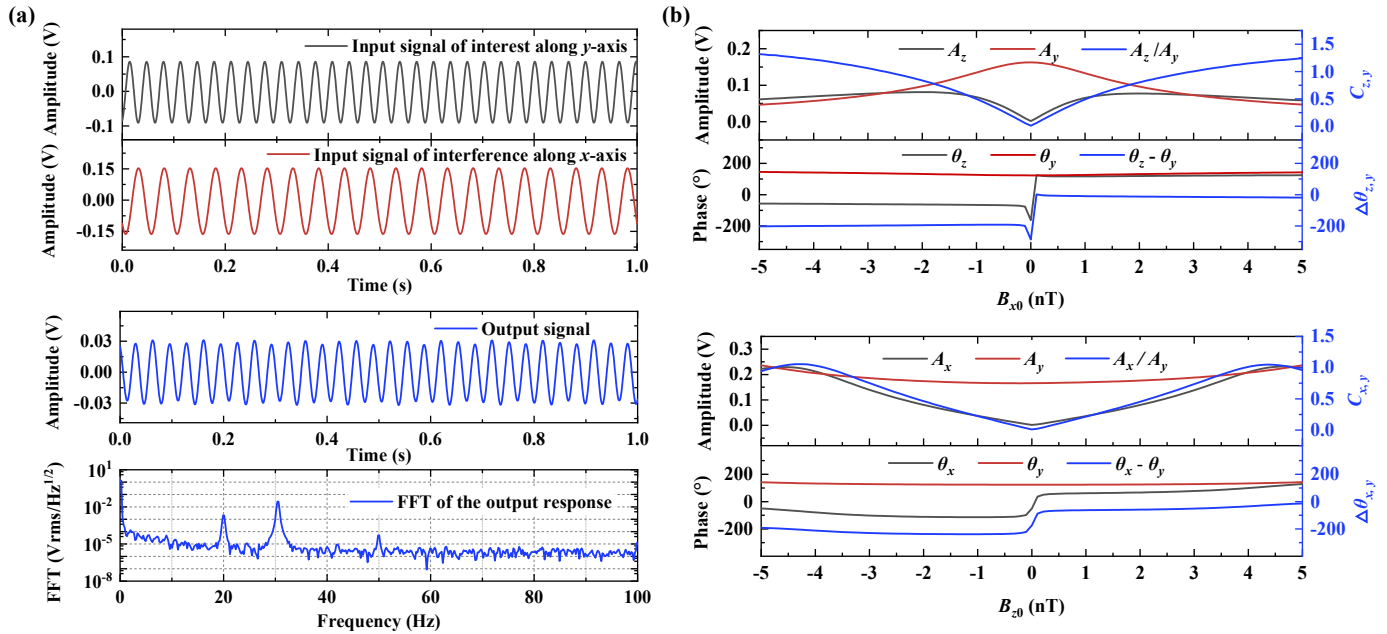


Figure 3. The output signal dependence on the background magnetic field. (a) Input signal in time-domain and the output signal in time-domain and frequency-domain. (b) Output response amplitude, cross-axis coupling coefficient, phase, and the phase difference for the sensitive and interference fields under the background magnetic field.

The phase delay was also influenced by the background field. Except for the phase reversals of θ_z and θ_x occurring at $B_{x0} = 0$ and $B_{z0} = 0$, respectively, the rates of change in θ_y were $20.2^\circ/5$ nT (with B_{x0} applied) and $18.8^\circ/5$ nT (with B_{z0} applied). Referring to the influence factors related to the phase of the magnetometer signal, except for the background magnetic field, there are other factors including the coils' inductance effect and the coupling between the coil and the magnetic shielding system. These factors are negligible under a small-magnitude and low-frequency magnetic field. Only the phase delay caused by the background magnetic field was considered.

The combined effect of the amplitude and phase delay would adversely influence the property of the magnetometer, including the sensitivity and the measurement accuracy of the magnetic field. At the same time, the phase delay is especially at a disadvantage for the capture of the instantaneous dynamic field and the magnetic source localization under the multi-sensor condition. Subsequently, only the positive-field measurement is given for the sake of brevity of the data.

To demonstrate how the interference field influenced the output signal, the dynamic response amplitude, coupling coefficient, and tilting degree variation with the background magnetic field were measured under a varied interference field amplitude. In Figure 4a, A_y decreased with increasing B_{x0} under different B_{z-rms} . $C_{z,y}$ and $\varphi_{z,y}$ showed a stronger cross-axis coupling effect with increasing B_{x0} and B_{z-rms} , while it was violated when B_{z-rms} was larger than 4 nT. When B_{z0} was applied as shown in Figure 4b, A_y tended to increase with B_{z0} under small B_{x-rms} , while the rule was violated under larger B_{x-rms} . It was found that the tilting degree $\varphi_{z,y}$ ($B_{x0} = 0.22$ nT, $B_{z-rms} = 0.01$ nT, and $\varphi_{z,y} = 8.49^\circ$; $B_{x0} = 0.22$ nT, $B_{z-rms} = 0.2$ nT, and $\varphi_{z,y} = 71.48^\circ$) increased faster than $\varphi_{x,y}$ ($B_{z0} = 0.22$ nT, $B_{x-rms} = 0.01$ nT, and $\varphi_{x,y} = 2.61^\circ$; $B_{z0} = 0.22$ nT, $B_{x-rms} = 0.2$ nT, and $\varphi_{x,y} = 42.84^\circ$) with increasing interference field, indicating that a background magnetic

field of the order of a hundred picotesla would cause severe tilting degrees of the axis with the field of interest.

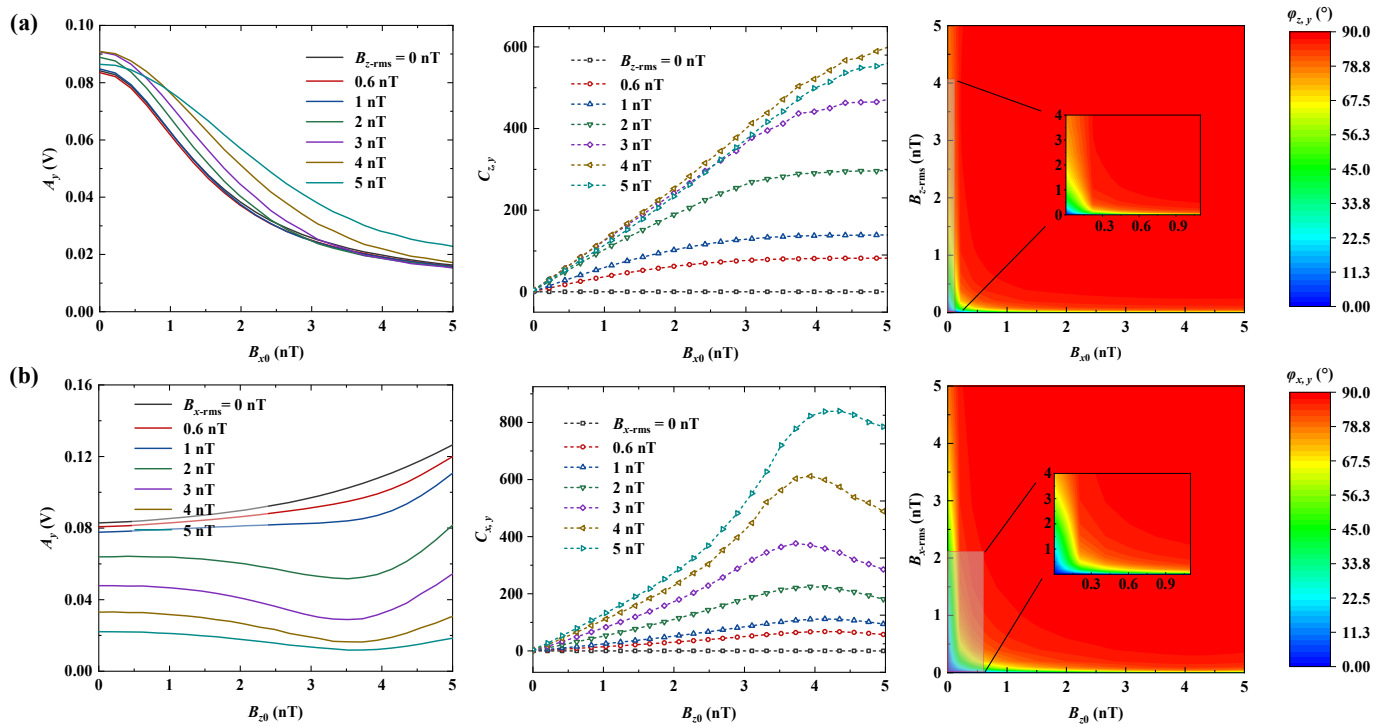


Figure 4. The output amplitude and coupling coefficient dependence on the background field under varied interference field amplitudes. (a) A_y , $C_{z,y}$, and $\phi_{z,y}$ dependence on B_{x0} . (b) A_y , $C_{x,y}$, and $\phi_{x,y}$ dependence on B_{z0} .

In addition, the frequency response was measured and is shown in Figure 5. The frequency ranged from 4 to 200 Hz, which covered the typical bandwidth of the SERF magnetometer. Figure 5a,b show that when B_{x0} was applied, A_y decreased and the cross-axis coupling effect enhanced monotonously with higher f_y . A_y tended to be less affected by f_y when the frequency was above 200 Hz, which was consistent with the derivation in Equation (8). The coupling effect was weaker with higher f_z and it tended to be less affected by f_z when the frequency was above 200 Hz. In addition, a larger interference field B_{z-rms} gave rise to a smaller A_y and stronger coupling effect at a certain frequency. When B_{z0} was applied, A_y and the cross-axis coupling effect showed a nonmonotonic variation with frequency due to the magnetic resonance. With increased f_y , A_y tended to increase first and then decrease, and it was less affected by f_y over 200 Hz, while the coupling effect did the opposite. With increased f_x , the coupling effect increased first and then decreased. It was less affected by f_x over 200 Hz.

According to $C_{z,y}$ and $C_{x,y}$ in Figure 5, the tilting degree of the sensitive axis was extracted, as shown in Figure 6. $\Phi_{z,y}$ was more affected by the higher frequency of the sensitive field while being less affected by the higher frequency of the interference field, indicating a more severe measurement error for the high-frequency signal of interest. For $\phi_{x,y}$, it increased monotonically with higher f_y and decreased with higher f_x under small B_{x-rms} (<1 nT), while it was violated when B_{x-rms} was larger.

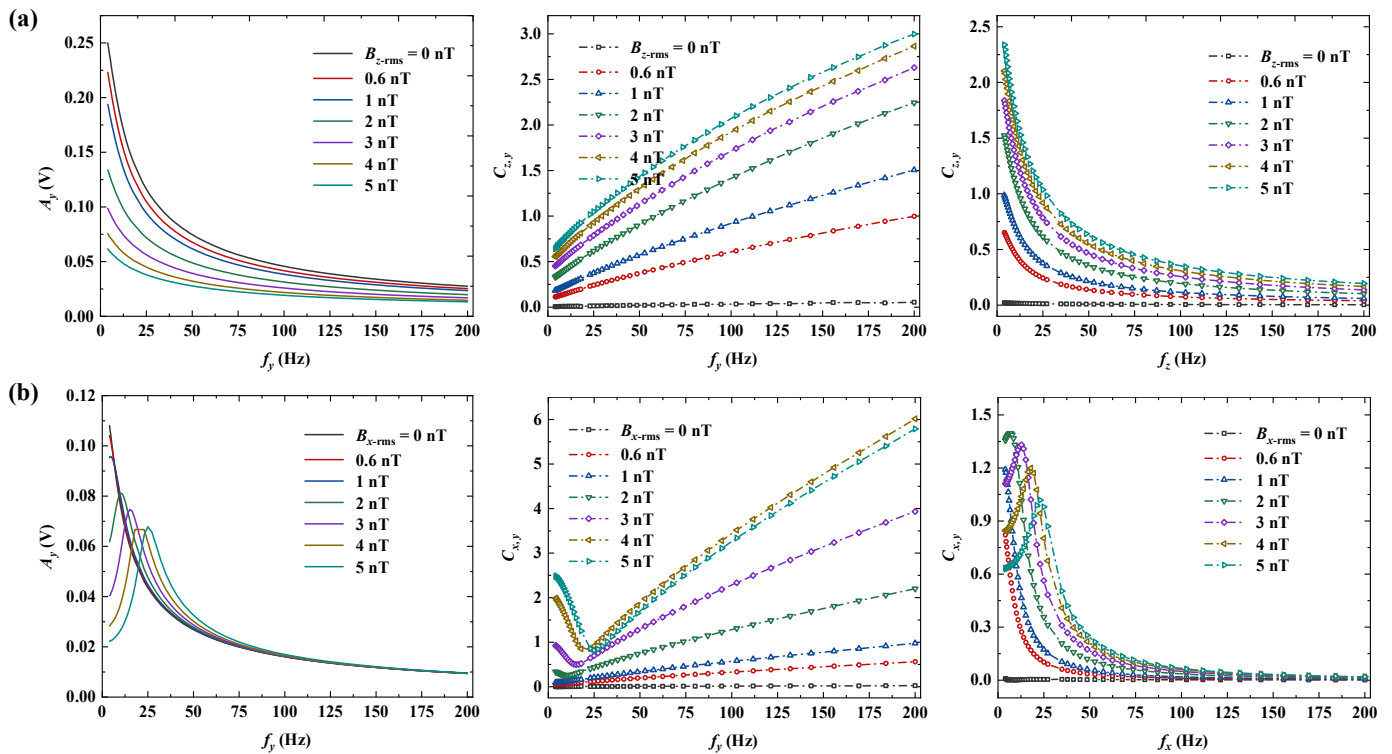


Figure 5. The amplitudes and coupling coefficients dependence on the frequency of the sensitive and interference field under varied interference field amplitude. (a) A_y and $C_{z,y}$ dependence on f_y ; $C_{z,y}$ dependence on f_z when B_{x0} was applied. (b) A_y and $C_{x,y}$ dependence on f_y ; $C_{x,y}$ dependence on f_x when B_{z0} was applied.

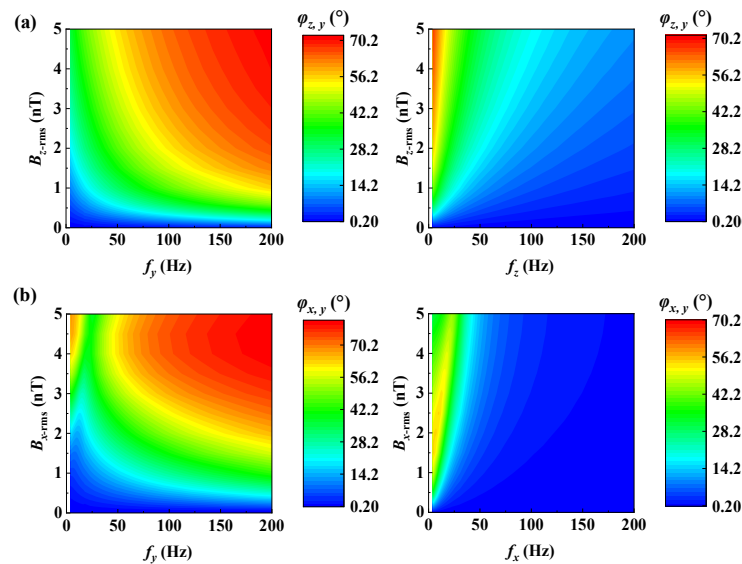


Figure 6. The tilting degree dependence on the frequency of the sensitive and interference field under varied interference field amplitude. (a) $\phi_{z,y}$ dependence on f_y and f_z when B_{x0} was applied. (b) $\phi_{x,y}$ dependence on f_y and f_x when B_{z0} was applied.

4.2. Suppression of the Cross-Axis Coupling Effect

Here, the in-phase components of the demodulated amplitude were used for PI closed-loop control and feedback of the compensation value to the axis with background field drift. The control flow diagram is given in Figure 7. To visibly compare the suppression effect before and after compensation, a magnetic field of nT order was applied. The background magnetic field $B_{x0} = 1$ nT (root-mean-square value, the same below) was set at 0.3 Hz

and the interference field $B_{z\text{-rms}} = 1.2 \text{ nT}$ was set at $f_z = 110 \text{ Hz}$, $\varphi_{z0} = 0$; the background magnetic field $B_{z0} = 3 \text{ nT}$ was set at 0.3 Hz and the interference field $B_{x\text{-rms}} = 3.5 \text{ nT}$ was set at $f_x = 110 \text{ Hz}$, $\varphi_{x0} = 0$.

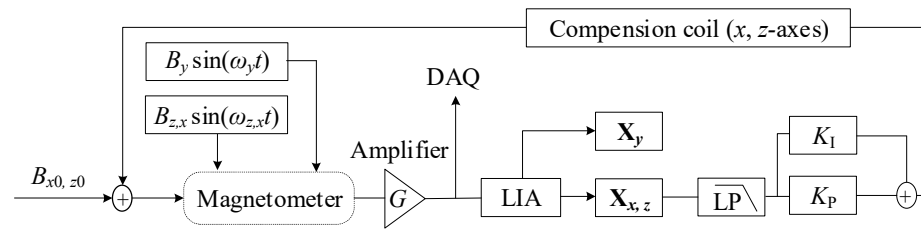


Figure 7. Flow diagram of the background magnetic field compensation for x - and z -axes, respectively. $X_{x,y,z}$ is the in-phase components of the demodulated amplitude.

The output voltage noise spectral density of the magnetometer was recorded in Figure 8a. Comparing the voltage signal before and after compensation, the cross-axis coupling effect was effectively suppressed by 1.5 times at 10–40 Hz. By transferring the collected voltage noise spectral density into magnetic field sensitivity, as shown in Figure 8b, the sensitivities for B_y improved from 3.9 to $2.7 \text{ fT/Hz}^{1/2}$ with B_{x0} applied and improved from 2.5 to $2.4 \text{ fT/Hz}^{1/2}$ with B_{z0} applied at 20–40 Hz. It showed a more obvious suppression effect for the background magnetic field along the x -axis, which was consistent with the results in Figure 4. As for the 0.3 Hz dynamic background field drift, it was compensated with the PI control phase delay of 2.36° (x -axis) and 2.97° (z -axis), while for a higher-frequency field drift at 18 Hz, there was a larger phase delay with 6.06° (x -axis) and 9.82° (z -axis) due to the higher bandwidth and higher order of the low-pass filter, giving rise to a poorer suppression effect.

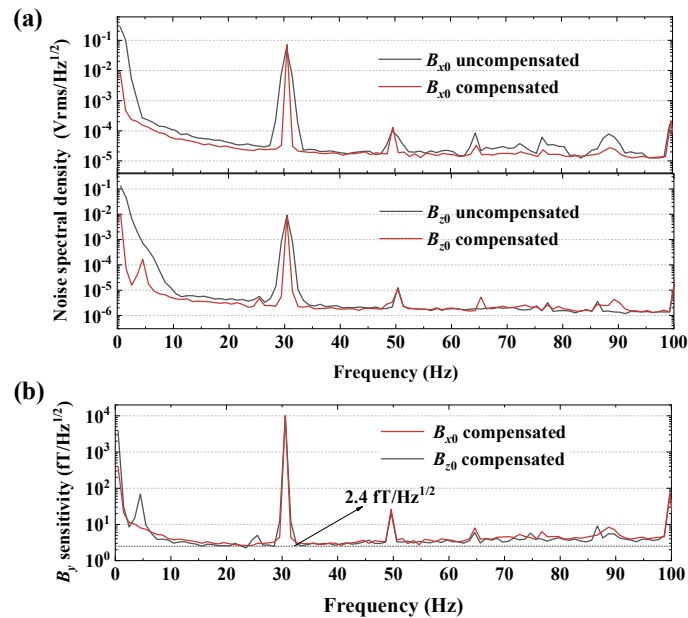


Figure 8. Noise spectral density and sensitivity with applied B_y at 30.5 Hz. (a) Voltage noise spectral density with background field along the x - and z -axes; (b) sensitivity of the magnetometer after compensation.

For static field compensation with no drift, the method illustrated above is also available. It is worth noting that the background field compensation only solves the cross-axis coupling problem aroused by the background field, while it did not restrain the A_y variation, due to the interference field, as shown in the denominator of Equation (15) and Figure 4 (see curves under $B_{x0} = 0$, $B_{z0} = 0$), which is a question worth further investigation.

5. Conclusions

In summary, the background-magnetic-field-evoked cross-axis coupling effect for a dual-beam SERF atomic magnetometer was analyzed and verified under the background field within ± 5 nT (typical SERF regime), indicating the adverse impact on the output signal. For the cross-axis coupling effect between z - and y -axes under a transverse background field B_{x0} , the coupling enhanced with increased B_{x0} and f_y , and the response amplitude A_y of the signal of interest tended to decrease with increased B_{x0} , so did the sensitivity, while for the effect between x - and y -axes under longitudinal background field B_{z0} , the coupling variation was nonmonotonic due to the magnetic resonance evoked by B_{z0} and B_y . Through the cross-axis magnetic field compensation method, the coupling effect was effectively suppressed by 1.5 times at 10–40 Hz. The method is applicable for static and low-frequency background field compensation, while the frequency of the interference and background fields should satisfy the condition of basic modulation and demodulation regulation because the two are multiple items, which limits the compensation bandwidth to dozens of Hz. The triaxial magnetic field closed-loop control technique with large-field modulation is efficient for field compensation with a wider frequency band and higher dynamic range, but it will sacrifice the sensitivity. An appropriate method should be selected according to practical application.

Author Contributions: Conceptualization, F.L. and B.L.; methodology, F.L.; validation, F.L., B.L. and J.L.; formal analysis, S.W.; investigation, N.X.; data curation, F.L.; writing—original draft preparation, F.L.; writing—review and editing, J.L.; project administration, J.L. and B.H.; funding acquisition, B.H. All authors have read and agreed to the published version of the manuscript.

Funding: This work was supported by the Natural Science Foundation of Beijing Municipality (Grant No. 4191002), Key R&D Program of Zhejiang, China (Grant No. 2020C01037).

Institutional Review Board Statement: Not applicable.

Informed Consent Statement: Not applicable.

Data Availability Statement: The data presented in this study are available on reasonable request from the corresponding author.

Conflicts of Interest: The authors declare no conflict of interest.

References

1. Allred, J.C.; Lyman, R.N.; Kornack, T.W.; Romalis, M.V. High-sensitivity atomic magnetometer unaffected by spin-exchange relaxation. *Phys. Rev. Lett.* **2002**, *89*, 130801. [[CrossRef](#)] [[PubMed](#)]
2. Li, R.; Baynes, F.N.; Luiten, A.N.; Perrella, C. Continuous high-sensitivity and high-bandwidth atomic magnetometer. *Phys. Rev. Appl.* **2020**, *14*, 064067. [[CrossRef](#)]
3. Kominis, I.K.; Kornack, T.W.; Allred, J.C.; Romalis, M.V. A subfemtotesla multichannel atomic magnetometer. *Nature* **2003**, *422*, 596–599. [[CrossRef](#)] [[PubMed](#)]
4. Rea, M.; Holmes, N.; Hill, R.; Boto, E.; Leggett, J.; Edwards, L.J.; Woolger, D.; Dawson, E.; Shah, V.; Osborne, J.; et al. Precision magnetic field modelling and control for wearable magnetoencephalography. *Neuroimage* **2021**, *241*, 118401. [[CrossRef](#)]
5. An, N.; Cao, F.; Li, W.; Wang, W.; Xu, W.; Wang, C.; Xiang, M.; Gao, Y.; Sui, B.; Liang, A.; et al. Imaging somatosensory cortex responses measured by OPM-MEG: Variational free energy-based spatial smoothing estimation approach. *iScience* **2022**, *25*, 103752. [[CrossRef](#)] [[PubMed](#)]
6. Hauk, O.; Stenroos, M.; Treder, M.S. Towards an objective evaluation of EEG/MEG source estimation methods—The linear approach. *Neuroimage* **2022**, *255*, 119177. [[CrossRef](#)]
7. Kornack, T.W.; Smullin, S.J.; Lee, S.K.; Romalis, M.V. A low-noise ferrite magnetic shield. *Appl. Phys. Lett.* **2007**, *90*, 223501. [[CrossRef](#)]
8. Romalis, M.V.; Dang, H.B. Atomic magnetometers for materials characterization. *Mater. Today* **2011**, *14*, 258–262. [[CrossRef](#)]
9. Colombo, S.; Lebedev, V.; Tonyushkin, A.; Pengue, S.; Weis, A. Imaging magnetic nanoparticle distributions by atomic magnetometry-based susceptometry. *IEEE Trans. Med. Imag.* **2020**, *39*, 922–933. [[CrossRef](#)]
10. Li, S.; Lu, J.; Ma, D.; Wang, K.; Gao, Y.; Sun, C.; Han, B. Measurement of nonorthogonal angles of a three-axis vector optically pumped magnetometer. *IEEE Trans. Instrum. Meas.* **2022**, *71*, 7001109. [[CrossRef](#)]

11. Brookes, M.J.; Boto, E.; Rea, M.; Shah, V.; Osborne, J.; Holmes, N.; Hill, R.M.; Leggett, J.; Rhodes, N.; Bowtell, R. Theoretical advantages of a triaxial optically pumped magnetometer magnetoencephalography system. *Neuroimage* **2021**, *236*, 118025. [[CrossRef](#)] [[PubMed](#)]
12. Boto, E.; Holmes, N.; Leggett, J.; Roberts, G.; Shah, V.; Meyer, S.S.; Munoz, L.D.; Mullinger, K.J.; Tierney, T.M.; Bestmann, S.; et al. Moving magnetoencephalography towards real-world applications with a wearable system. *Nature* **2018**, *555*, 657–661. [[CrossRef](#)] [[PubMed](#)]
13. Hill, R.; Boto, E.; Holmes, N.; Hartley, C.; Seedat, Z.; Leggett, J.; Roberts, G.; Shah, V.; Tierney, T.; Woolrich, M.; et al. A tool for functional brain imaging with lifespan compliance. *Nat. Commun.* **2019**, *10*, 4785. [[CrossRef](#)] [[PubMed](#)]
14. Yan, Y.; Lu, J.; Zhou, B.; Wang, K.; Liu, Z.; Li, X.; Wang, W.; Liu, G. Analysis and correction of the crosstalk effect in a three-axis SERF atomic magnetometer. *Photonics* **2022**, *9*, 654. [[CrossRef](#)]
15. Piil-Henriksen, J.; Merayo, J.M.G.; Nielsen, O.V.; Petersen, H.; Petersen, J.R.; Primdahl, F. Digital detection and feedback fluxgate magnetometer. *Meas. Sci. Technol.* **1996**, *7*, 897–903. [[CrossRef](#)]
16. Zhang, R.; Ding, Y.; Yang, Y.; Zheng, Z.; Chen, J.; Peng, X.; Wu, T.; Guo, H. Active magnetic-field stabilization with atomic magnetometer. *Sensors* **2020**, *20*, 4241. [[CrossRef](#)]
17. Iivanainen, J.; Zetter, R.; Grön, M.; Hakkarainen, K.; Parkkonen, L. On-scalp MEG system utilizing an actively shielded array of optically-pumped magnetometers. *Neuroimage* **2019**, *194*, 244–258. [[CrossRef](#)]
18. Cohen-Tannoudji, C.; Dupont-Roc, J.; Haroche, S.; Laloë, F. Diverses résonances de croisement de niveaux sur des atomes pompés optiquement en champ nul II. Applications à la mesure de champs faibles. *Rev. Phys. Appl.* **1970**, *5*, 102–108. [[CrossRef](#)]
19. Borna, A.; Iivanainen, J.; Carter, T.R.; McKay, J.; Taulu, S.; Stephen, J.; Schwindt, P.D.D. Cross-axis projection error in optically pumped magnetometers and its implication for magnetoencephalography systems. *Neuroimage* **2022**, *247*, 118818. [[CrossRef](#)]
20. Jiang, M.; Xu, W.; Li, Q.; Wu, Z.; Suter, D.; Peng, X. Interference in atomic magnetometry. *Adv. Quantum Technol.* **2020**, *3*, 2000078. [[CrossRef](#)]
21. Sakamoto, Y.; Bidinosti, C.P.; Ichikawa, Y.; Sato, T.; Ohtomo, Y.; Kojima, S.; Funayama, C.; Suzuki, T.; Tsuchiya, M.; Furukawa, T.; et al. Development of high-homogeneity magnetic field coil for ^{129}Xe EDM experiment. *HyInt* **2015**, *230*, 141–146. [[CrossRef](#)]
22. Ding, Z.; Huang, Z.; Pang, M.; Han, B. Iterative optimization algorithm to design bi-planar coils for dynamic magnetoencephalography. *IEEE Trans. Ind. Electron.* **2022**, *70*, 2085–2094. [[CrossRef](#)]
23. Li, Y.; Xu, J.; Kang, X.; Fan, Z.; Dong, X.; Gao, X.; Zhuang, S. Design of highly uniform three-dimensional square magnetic field coils for external magnetic shielding of magnetometers. *Sens. Actuator A Phys.* **2021**, *331*, 113037. [[CrossRef](#)]
24. Lu, Y.; Yang, Y.; Zhang, M.; Wang, R.; Jiang, L.; Qin, B. Improved square-coil configurations for homogeneous magnetic field generation. *IEEE Trans. Ind. Electron.* **2022**, *69*, 6350–6360. [[CrossRef](#)]
25. Yan, Y.; Lu, J.; Zhang, S.; Lu, F.; Yin, K.; Wang, K.; Zhou, B.; Liu, G. Three-axis closed-loop optically pumped magnetometer operated in the SERF regime. *Opt. Express* **2022**, *30*, 18300–18309. [[CrossRef](#)]
26. Ding, Z.; Yuan, J.; Lu, G.; Li, Y.; Long, X. Three-axis atomic magnetometer employing longitudinal field modulation. *IEEE Photon. J.* **2017**, *9*, 5300209. [[CrossRef](#)]
27. Jiang, L.; Liu, J.; Liang, Y.; Tian, M.; Quan, W. A single-beam dual-axis atomic spin comagnetometer for rotation sensing. *Appl. Phys. Lett.* **2022**, *120*, 074101. [[CrossRef](#)]
28. Seltzer, S.J.; Romalis, M.V. Unshielded three-axis vector operation of a spin-exchange-relaxation-free atomic magnetometer. *Appl. Phys. Lett.* **2004**, *85*, 4804–4806. [[CrossRef](#)]
29. Ledbetter, M.P.; Savukov, I.M.; Acosta, V.M.; Budker, D.; Romalis, M.V. Spin-exchange-relaxation-free magnetometry with Cs vapor. *Phys. Rev. A* **2008**, *77*, 033408. [[CrossRef](#)]
30. Ma, D.; Lu, J.; Fang, X.; Yang, K.; Wang, K.; Zhang, N.; Han, B.; Ding, M. Parameter modeling analysis of a cylindrical ferrite magnetic shield to reduce magnetic noise. *IEEE Trans. Ind. Electron.* **2022**, *69*, 991–998. [[CrossRef](#)]
31. Ma, D.; Lu, J.; Fang, X.; Wang, K.; Wang, J.W.; Zhang, N.; Chen, H.; Ding, M.; Han, B. Analysis of coil constant of triaxial uniform coils in Mn–Zn ferrite magnetic shields. *J. Phys. D* **2021**, *54*, 275001. [[CrossRef](#)]